

Article

# Predicting Far-Field Noise Generated by a Landing Gear Using Multiple Two-Dimensional Simulations

Sultan Alqash <sup>1,2,\*</sup>, Sharvari Dhote <sup>1</sup> and Kamran Behdinin <sup>1</sup>

<sup>1</sup> Department of Mechanical and Industrial Engineering, University of Toronto, 5 King's College Road, Toronto, ON M5S 3G8, Canada; sharvari.dhote@mail.utoronto.ca (S.D.); behdinin@mie.utoronto.ca (K.B.)

<sup>2</sup> Mechanical Engineering Department, Taibah University, Al-Madinah Al-Munawarah P.O. Box. 344, Saudi Arabia

\* Correspondence: sultan.alqash@mail.utoronto.ca or sultan.eng2019@gmail.com

Received: 14 August 2019; Accepted: 18 October 2019; Published: 23 October 2019



**Featured Application:** Far-field noise prediction of flow past complex multi-component structures.

**Abstract:** In this paper, a new approach is proposed to predict the far-field noise of a landing gear (LG) based on near-field flow data obtained from multiple two-dimensional (2D) simulations. The LG consists of many bluff bodies with various shapes and sizes. The analysis begins with dividing the LG structure into multiple 2D cross-sections (C-Ss) representing different configurations. The C-Ss locations are selected based on the number of components, sizes, and geometric complexities. The 2D Computational Fluid Dynamics (CFD) analysis for each C-S is carried out first to obtain the acoustic source data. The Ffowcs Williams and Hawkings acoustic analogy (FW-H) is then used to predict the far-field noise. To compensate for the third dimension, a source correlation length (SCL) is assumed based on a perfectly correlated flow. The overall noise of the LG is calculated as the incoherent sum of the predicted noise from all C-Ss. Flow over a circular cylinder is then studied to examine the effect of the 2D CFD results on the predicted noise. The results are in good agreement with reported experimental and numerical data. However, the Strouhal number ( $St$ ) is over-predicted. The proposed approach provides a reasonable estimation of the LG far-field noise at a low computational cost. Thus, it has the potential to be used as a quick tool to predict the far-field noise from an LG during the design stage.

**Keywords:** aeroacoustics; landing gear; two-dimensional; multiple two-dimensional; far-field noise; FW-H

## 1. Introduction

Aircraft noise has been recognized as a significant environmental problem since the 1950s. However, due to the development of quieter engines, Airframe Noise (AFN) has become the dominant source of noise during the landing phase [1]. Among the airframe components, the landing gears (LGs) are considered one of the main sources of noise emitted during the approach-to-land phase of flight. In the last 40 years, aeroacoustics became an important research field to accelerate AFN reduction. Both U.S. and European governments have set stringent targets to minimize the AFN [2]. To fulfill high design standards, new aircraft designs demand efficient AFN prediction techniques to assess the noise impact. Thus, multi-fidelity approaches are required to enable efficient and accurate aircraft noise assessment at different design stages [3]. The accuracy of noise prediction techniques is attributed to various factors, including turbulence modelling and/or acoustic analogy implementation and boundary conditions [4–9].

The direct numerical simulation (DNS) of complex three-dimensional (3D) aircraft systems, such as the LGs, is computationally expensive. This is because the 3D model needs high spatial and temporal resolutions to resolve the wide range of energy and length scales between the flow and acoustic fields. Therefore, an efficient two-step hybrid computational aeroacoustics (CAA) approach was proposed, where the flow and the acoustic fields are computed using two independent solvers [8]. In the last decade, noise generated due to flow past a simplified LG geometry has been extensively investigated using hybrid CAA approaches. The numerical results were validated with experiments through benchmark problems for airframe noise computations (BANC) workshops [10–14]. The BANC workshops focus on improving the far-field noise prediction accuracy of the 3D simulations and reducing the computation time. There are a few semi-empirical tools developed to facilitate the noise prediction of the LG during the design stage [3,7]. Among these, the Landing Gear Model and Acoustic Prediction tool (LGMAP) has been developed for a quick noise estimate of the LG [15]. However, lower fidelity approaches are essential to predict the flow and acoustic quantities with better computational efficiency and reasonable accuracy.

The two-dimensional (2D) Computational Fluid Dynamics (CFD) analysis provides a faster way to predict the near-field data. A few studies investigated the validity of the 2D simulations to predict the far-field noise of the flow around a circular cylinder [16–24]. It was observed that the amplitude of the fluctuating forces around the cylinder and their associated noise is highly dependent on the flow coherence level (i.e., vortex shedding pattern) along the spanwise direction. Although, the vortex shedding being a 3D flow quantity, it was found to be fully correlated along a certain length, which was typically less than 10 times the cylinder diameter [18,25]. To predict the far-field noise from the 2D near-field flow data, the effect of the third dimension can be compensated by assigning a source correlation length (SCL) [25–28].

The experimental investigations of flow past a circular cylinder conducted by Revell et al. [29] were widely used as a benchmark validation of the hybrid CAA methods. Many studies showed that different correlation lengths were obtained in accordance with the Reynolds numbers (Re) based on the cylinder diameter [24–30]. At low Re, Morkovin [24] observed that the flow was homogeneous along the spanwise direction with a correlation length around 15 to 18 times the circular diameter. This high correlation length is due to the fact that the 3D flow barely occurred at this range of the low Re. However, the correlation length dramatically decreased to two to four times the circular diameter for Re above  $10^5$  [20–22]. As the boundary layer becomes fully turbulent, the correlation length decreases to 1 to 1.25 times the circular diameter [20]. The results of the 2D simulations of flow past a circular cylinder over-predicted the Strouhal number (St) and the peak amplitude [22]. Overall, the 2D results might over-predict/under-predict some of the flow quantities, but the acoustic amplitude was found to be highly dependent on the assumed value of the SCL.

This paper presents a new approach for a quick and reasonable estimate of the far-field noise generated due to flow past an LG utilizing multiple cross-sectional 2D flow simulations. The SCL parameter is used to account for the flow three-dimensionality into the acoustic calculations. The first part of this work discusses the influence of the SCL on the far-field noise prediction of a classical flow problem at  $Re = 9.0 \times 10^4$  using 2D flow simulations. The second part describes the idea of obtaining the multiple LG cross-sections (C-Ss) and the procedure to calculate the far-field noise for a simplified nose LG. The following part presents the LG C-S acoustic results and discussion. Finally, the conclusions section highlights the advantages and limitations of the developed approach.

## 2. Flow Past a Circular Cylinder

The LG is a complex structure consisting of many components with different configurations and dimensions. Most of the LG components, such as shock strut, drag strut, and wheel axle, are of cylindrical shape. Thus, the flow past a circular cylinder is examined by 2D simulations performed using ANSYS FLUENT. Then, the effect of the SCL on the acoustic prediction is tested. In FLUENT, the SCL can be chosen to calculate the 3D far-field noise when the 2D flow computation is used.

The Ffowcs Williams and Hawkings (FW-H) integration is evaluated over the entire length (SCL) in the depth-wise direction. In that case, the flow is assumed to be fully correlated along the assumed SCL, where the 2D CFD source data is repeated periodically. Both the flow and acoustic results are then validated with the available experimental and numerical data in the literature.

2.1. The 2D Flow and Acoustic Numerical Setup

The 2D flow computational domain is modelled using ANSYS Workbench. The inlet and outlet boundaries are extended  $8.5D$  and  $20.5D$  from the centerline of the cylinder diameter ( $D = 0.019$  m) upstream and downstream, respectively. The top and bottom boundaries are located at  $10.5D$  in both directions from the cylinder center. The entire domain is then discretized using an unstructured mesh with triangular cells. However, near to the cylinder wall, a structured mesh with rectangular elements is used to capture the boundary layer (BL). The boundary conditions are assigned as follows: velocity inlet,  $U_{in} = 69.2$  m/s and pressure outlet,  $P_{gauge} = 0$  Pa to prevent any backflow into the domain. Both the flow density,  $\rho = 1.225$  kg/m<sup>3</sup> and viscosity,  $\mu = 1.7894 \times 10^{-5}$  kg/m.s are kept as the default values for the air. As a result, the calculated  $Re = (U_{in}D\rho)/\mu = 9.0 \times 10^4$  and Mach number,  $M = U_{in}/c_o = 0.2$ , where the speed of sound in the air,  $c_o = 340$  m/s.

Since this  $Re$  is in the subcritical flow regime (i.e., the wake is fully turbulent), the Large Eddy Simulation (LES) turbulence model is used. In this study, the importance of capturing the quasi-2D flow mechanisms is evaluated. The far-field noise is computed based on the 2D near-field flow data, and the corresponding acoustic results are validated with the experimental data of Revell et al. [29]. The receiver is located at  $128D$  away from the center of the cylinder and perpendicular to the flow direction. The SCL is assumed based on the experimental observations from previous studies [21,29]. The mesh sensitivity study is carried out by changing the maximum face size for the computational domain. Three different meshes are generated, and their characteristics are summarized in Table 1. Since the mean drag coefficient results for medium and fine grids are comparable, the medium mesh is used for all the remaining computations.

Table 1. Mesh properties obtained for a circular cylinder at  $Re = 9.0 \times 10^4$  in FLUENT.

Mesh Size	Max. Face Size (m)	Wall Edge Sizing	Near-Wall Inflation Definition			Total No. of Elements	Mean Drag Coefficient $\bar{C}_d$	Computed OASPL (dB)	% Error (Exp. by Revell et al. [29] 100 dB)
		Element Size (m) (No. of Cells)	First Layer Height (m)	Max. No. of Layers	Growth Rate (%)				
Coarse	$5.0 \times 10^{-3}$					$3.2313 \times 10^4$	0.733	101.094	1.088
Medium	$3.0 \times 10^{-3}$	$3.0 \times 10^{-4}$ (200 cells)	$4.2 \times 10^{-6}$	70	1.2 (20%)	$6.3187 \times 10^4$	0.782	100.874	0.870
Fine	$2.0 \times 10^{-3}$					$1.2483 \times 10^5$	0.746	101.28	1.122

2.2. The Validation of the 2D Flow Results

The present numerical results are validated with the available experimental and numerical data. Table 2 presents the comparison of different flow quantities, such as the  $St$  and mean drag coefficient ( $\bar{C}_d$ ). It is observed that the turbulence model considerably affects the predicted  $St$  and values. Also, all the outcomes of the 2D simulations over-predict the calculation of the fluctuating flow quantity,  $St$  and underestimated the mean flow quantity,  $\bar{C}_d$ . The over-prediction of the  $St$  was discussed by Casalino and Jacob [28], which has a direct impact on the predicted noise. They demonstrated that the shedding frequency resulted from the 2D simulation is high due to the difference between higher Reynolds stresses and shorter recirculating regions behind the body.

**Table 2.** Comparison of the obtained flow quantities with experimental, 2D, and 3D numerical results for a circular cylinder at  $Re = 9.0 \times 10^4$ .

Flow Quantities		St	$\bar{C}_d$ †
Experimental Data		0.180–0.191 (Norberg [21])	1.0–1.4 (Cantwell et al. [31])
Turbulence Model	2D	$k-\omega$ SST Orselli et al. [22]	0.247
		$k-\omega$ SST Brentner et al. [27]	0.227
		LES—Present study	0.240
	3D	LES Orselli et al. [22]	0.191
			1.08

† Experimentally the  $\bar{C}_d = 1.312$  (for smooth cylinder) and  $\bar{C}_d = 0.943$  (for rough cylinder) when the  $M = 0.2$  and  $Re = 8.9 \times 10^4$  [29].

The pressure coefficient,  $C_p$ , distribution around the upper surface of the cylinder is monitored and validated with the analytical solution of an inviscid flow and the experimental results of Cantwell et al. [31] at  $Re = 1.4 \times 10^5$ . The  $C_p$  values show good agreement with the experimental and the numerical results, particularly at the front surface of the cylinder, as shown in Figure 1. However, the present 2D LES result over-predicts the measured  $C_p$  in the back of the cylinder compared to the 2D Shear Stress Transport (SST) and 3D LES data [22]. Overall, the flow quantities are reasonably reproduced using the 2D CFD simulation with less computational cost compared to the 3D simulation [22,32–39].

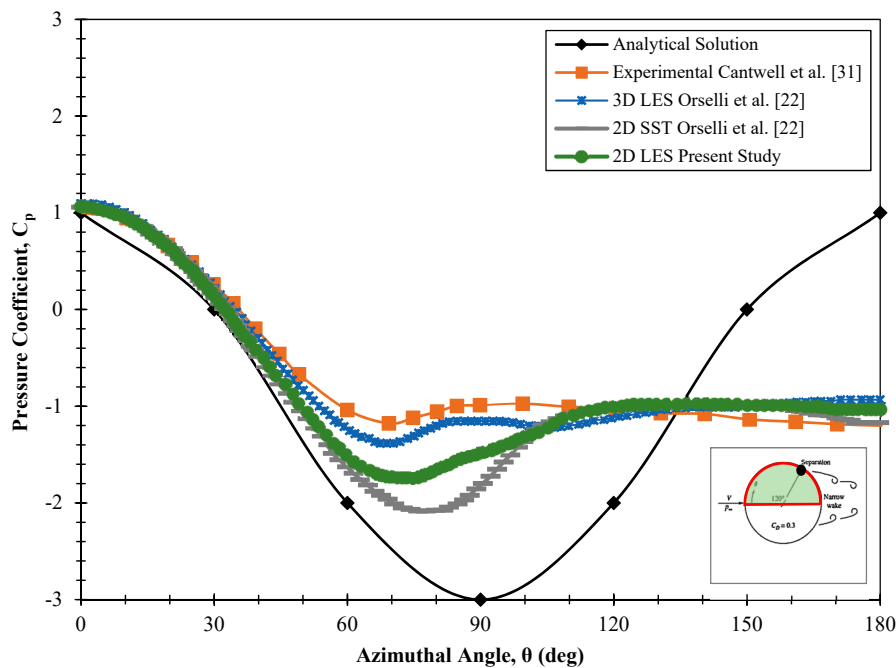


**Figure 1.** Pressure coefficient profile around the upper surface of the circular cylinder at  $Re = 9.0 \times 10^4$ .

Indeed, the present 2D LES simulation requires extremely less computational efforts compared with that of the 3D LES simulation performed by Orselli et al. [22]. For instance, the 2D simulation requires approximately 10 h CPU time (single-core) to complete  $28 \times 10^3$  time steps (the time step size,  $\Delta t = 5.0 \times 10^{-6}$  s). However, the 3D simulation required 35 days to execute  $50 \times 10^3$  time steps ( $\Delta t = 3.4 \times 10^{-6}$  s) using 16 parallel multi-core CPU [22]. This huge difference in computational cost is expected to increase when performing the same analysis on a complex LG structure.

### 2.3. Acoustic Results Validation

The effect of the grid densities on the Overall Sound Pressure Level (OASPL) is already investigated and presented in Table 1. It is noted that the OASPL value with  $SCL = 5.0D$  for all the three mesh sizes is in good agreement with the measured experimental data obtained by Revell et al. [29]. Norberg [21]

observed experimentally that the flow was fully correlated along  $SCL_{Exp.} \approx 3.16D$ . This  $SCL_{Exp.}$  value was utilized by Oreslli et al. [22] besides the other four values,  $2.5D$ ,  $5.0D$ ,  $10.0D$ , and  $25.3D$ . They concluded that the  $SCL = 5.0D$  was in good quantitative agreement with the OASPL experimental data [29]. In the current study, the same observation is also noticed. Note that the acoustic data is extracted from the 2D near-field flow, while the acoustic source is coincident with the outer surface of the cylinder.

Figure 2 presents the comparison of the predicted Sound Pressure Level (SPL) with the experimental data [29] and similar numerical acoustic results obtained from previous studies [27,40]. In these studies, the near-field flow data were obtained using different CFD solvers. For example, Brentner et al. [27] used an in-house CFD code based on the SST turbulence model to collect near-field data, and the far-field noise is calculated using the FW-H analogy. However, Evdokimov et al. [40] obtained the acoustic results using the Curle acoustic analogy implemented in the OpenFOAM to predict the far-field pressure fluctuations. In the present study, the built-in FW-H acoustic solver in FLUENT is used to compute the far-field noise.

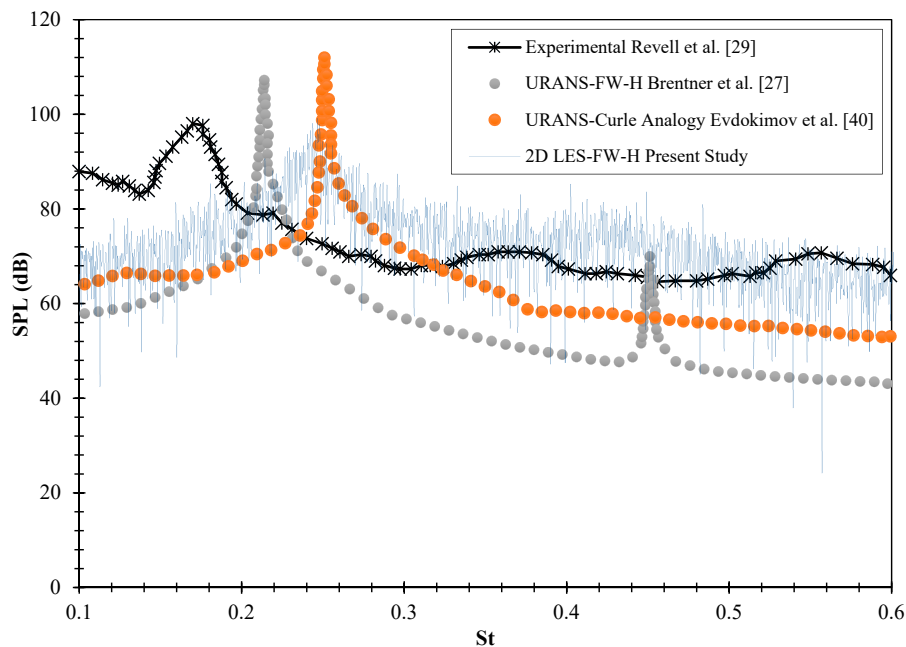


**Figure 2.** Comparison of the predicted Sound Pressure Level (SPL) with the experimental and computed acoustic results for a circular cylinder at  $Re = 9.0 \times 10^4$ .

As mentioned earlier, when the  $Re$  is high, the wake becomes fully turbulent, and thus, the fundamental motion of the von Karman vortex street can be visible. Nevertheless, this motion is superimposed by the spanwise velocity fluctuations characterized by different frequencies and phases. These fluctuations affect the surface pressure, which then influences the far-field noise signature by altering the spectral broadening of the tonal noise [21]. Although the vortex shedding frequency is over-predicted, the peak amplitude of the SPL of the present study has a better matching with the experimental data. Based on that, the 2D LES turbulence model can capture the essential flow characteristics compared to other turbulence models. Interestingly, the present 2D LES successfully reproduces the broadening of the tonal noise, as shown in Figure 2. Therefore, the LES turbulence model is utilized to solve all the 2D simulations in this work. In general, the turbulence model, acoustic analogy, and the assumed SCL highly influence the predicted far-field noise. This study provides insights to locate the C-Ss, and then the SCL is assumed accordingly to obtain the source data for the far-field noise calculations of the proposed approach.

### 3. Proposed Approach for the LG Far-Field Noise Prediction

As demonstrated earlier, this work presents a new approach to predict the far-field noise based on multiple 2D near-field flow data obtained using multiple LG C-Ss. To obtain these 2D C-Ss, different locations are selected based on the LG complexity, such as the number of components, sizes, and orientations. Thus, the number of the 2D horizontal planar cuts along the LG would vary. This work is mainly focused on proving the concept of the proposed method. The far-field noise is predicted using the FW-H acoustic analogy. To predict the far-field noise from obtained 2D near-field flow data, the missing data along the span can be compensated by assigning an SCL. For a variety of bluff body shapes at moderate to high  $Re$ , the flow was found to be fully correlated just along a few body diameters [39,41–43].

The size of the computational domain for each C-S is specified individually based on the corresponding  $L_a$ . The 2D CFD analysis is then carried out first for each C-S to generate the near-field flow data. Ultimately, the total power spectral density (PSD) is calculated as the summation of all the noises propagated from each 2D C-S. The proposed methodology is applied to the Landing Gear nOise database and CAA validatiON (LAGOON), a simplified nose landing gear (NLG), which was considered a benchmark problem during the second BANC workshop [6]. The LAGOON NLG experimental data [12] and the 3D numerical results [44] are used to validate the proposed method. One of the advantages of the proposed approach is that the CFD analysis of each 2D C-S is carried out individually. Thus, the domain size, mesh generation process, and computational time are considerably reduced compared to the corresponding 3D LG model.

In our approach, the SCL is assumed in accordance with the calculated local Reynolds number,  $Re^*$ , based on the characteristic length,  $L_a$ , of each C-S. In addition, any major change in the features of the C-S geometry altering the flow characteristics is taken into account to assume the SCL. In fact, in aerodynamic flow, besides the 3D nature of vortex shedding, there are two types of irregularities affecting the level of coherence [45]. For instance, disturbing the flow homogeneity could be triggered by either cylinder irregularity or flow irregularity or a combination of them. The first type is subdivided into surface irregularities, section irregularities, and spanwise irregularities. The latter can be classified into end effects, axis deviation, and variable local radius (For more details refer to [45]). The summary of steps for the proposed approach is illustrated for both flow and acoustic domains.

#### A. The flow domain setup:

1. Divide the 3D LG model into multiple slices with different configurations and dimensions, similar to Figure 3. For long aspect ratio (i.e., length-to-diameter ratio,  $AR > 3$ ) bluff bodies, mainly located at the upper part of the LG, a single C-S for each is sufficient to capture the flow behaviours. However, the lower part of the LG consists of bulky components with short aspect ratio; thus, at least three horizontal planar cuts should be taken. For example, one of the C-Ss is placed at the middle of the axle-wheel region, and the other two are located symmetrically at the upper and lower portion of the wheels. The latter two C-Ss should be placed away from the upper and lower wheels' circumference zones as well as the inner cavities' rim to avoid the flow separation points.
2. Model and size the 2D computational domain for each C-S separately based on the corresponding  $L_a$ .
3. Discretize each domain using a hybrid mesh, where an unstructured mesh is used for the entire domain, and a structured mesh is used around the body to capture the BL.
4. Simulate each 2D domain individually using the CFD solver.
5. Extract and save all the necessary near-field flow data such as the unsteady surface pressure after the statistically steady state is established to be used as an input for the acoustic calculations in the next step.

#### B. The acoustic calculations:

1. Specify the outer surface of each resulting C-S as an acoustic source.
2. Locate the receiver for each individual domain right above the body and at a distance relative to the microphone location in the experiment.
3. Run the simulation for many time steps to acquire enough samples for a recorded acoustic pressure signal.
4. In order to calculate the far-field noise from the 2D flow data, the SCL is assumed based on the object geometry, its associated flow characteristics, and the available experimental data or empirical formulas.
5. The overall far-field noise of the LG is calculated by summing up all the noise contributions from each C-S.

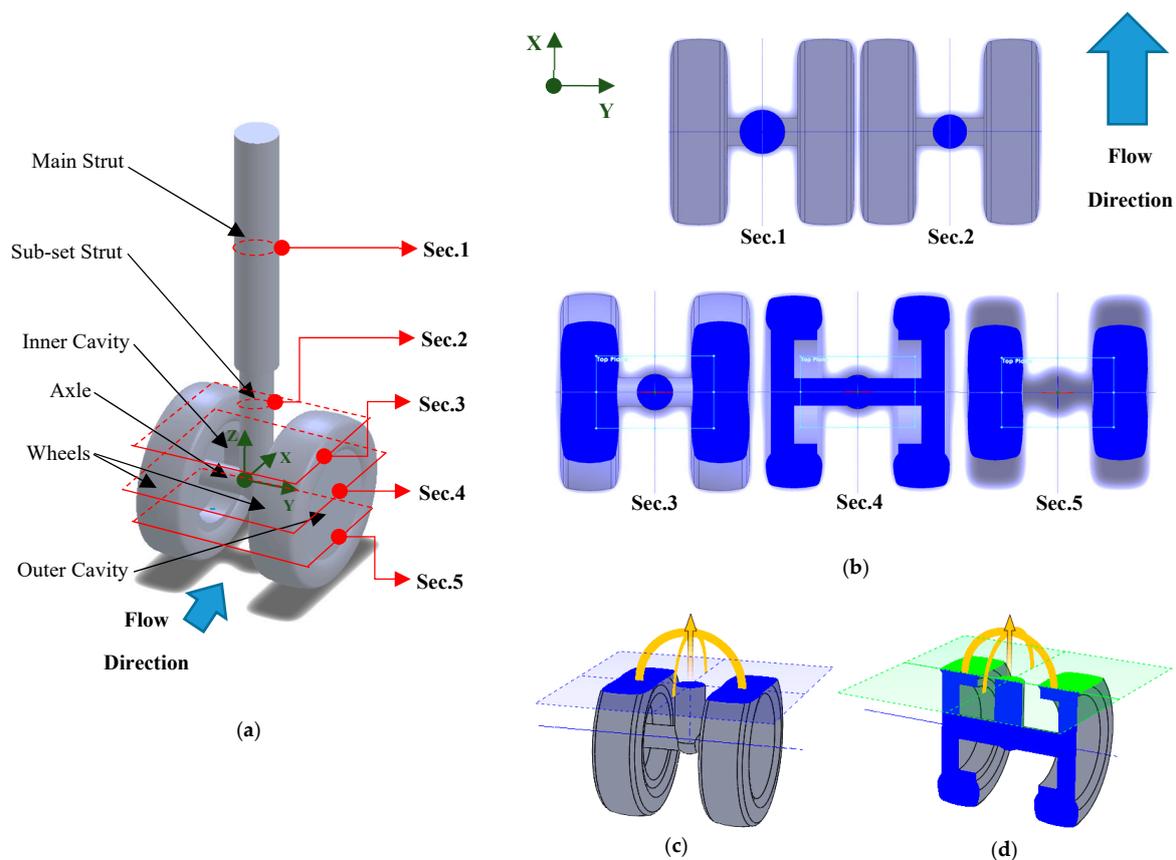


**Figure 3.** The 3D Landing Gear nOise database and CAA validation (LAGOON) nose landing gear (NLG) model with: (a) locations of section planes; (b) 2D cross-sections (C-Ss); (c,d) illustrations for the location of Sec.3.

Figure 3a,b show the 3D model of the LAGOON NLG with the locations of the C-S's at different heights along the Z-axis and the resulting C-Ss, respectively. Below is a description of the C-Ss used in the CFD computations.

- The first plane is located along the main strut to capture the flow structures and noise generated around the vertical circular cylinder.
- The second plane is taken at the next sub-set strut component, which also has a cylindrical geometry but with a smaller diameter. Thus, this C-S would capture the changes in flow behaviour.
- The third plane is placed at the upper rim of the outer cavities, as shown in Figure 3c,d, so that the essential flow characteristics of the upper part of the two wheels can be addressed.
- The fourth plane represents a more complex C-S at the middle of the axle-wheels components.

- Finally, the fifth plane is located at the lower part of the two wheels along the lower rim of the outer cavities. It has a shape similar to the third C-S but without the circular component in between the two wheels.

These five primary C-Ss are defined to capture different flow behaviours and examine their associated noise, named as: Sec.1, Sec.2, Sec.3, Sec.4, and Sec.5, respectively.

### 3.1. The 2D CFD Setup for the LAGOON NLG

After the number of C-Ss is set for the different components and configurations, the dimensions are obtained using CAD software accordingly. The full 3D LAGOON NLG is modelled using SolidWorks to facilitate extracting the dimensions of each C-S. Then, the flow computational domain is designed separately for each C-S using ANSYS Workbench. Figure 4 shows the dimensions and boundary conditions applied to the circular geometry of Sec.1 and Sec.2. However, in Sec.3, Sec.4, and Sec.5, half of their characteristic lengths are used to reduce the size of the domain.

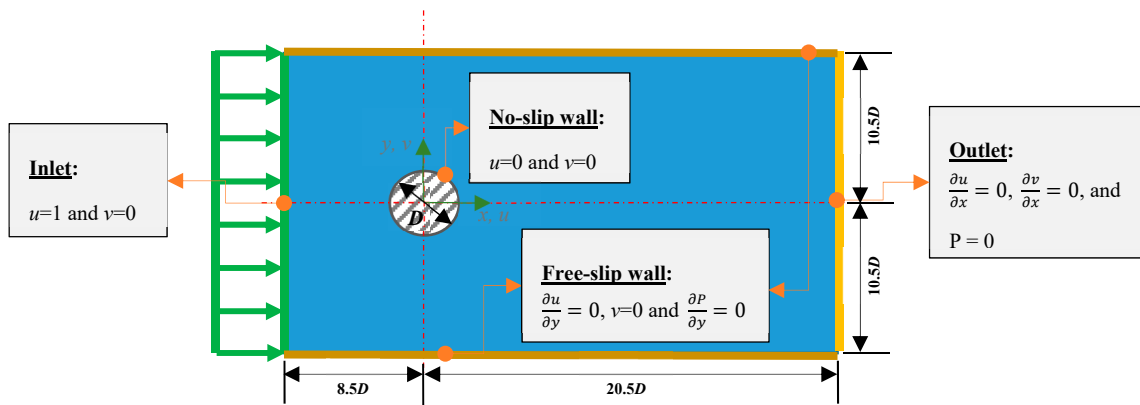


Figure 4. Schematic of the 2D computational domain size and boundary conditions for Sec.1 and Sec.2.

Figure 5 illustrates the mesh configurations of the 2D computational domain, where the hybrid mesh method is utilized, as mentioned earlier. The unstructured mesh is used to discretize the entire domain, while the structured mesh is used around the contour of each C-S to capture the BL and flow separation.

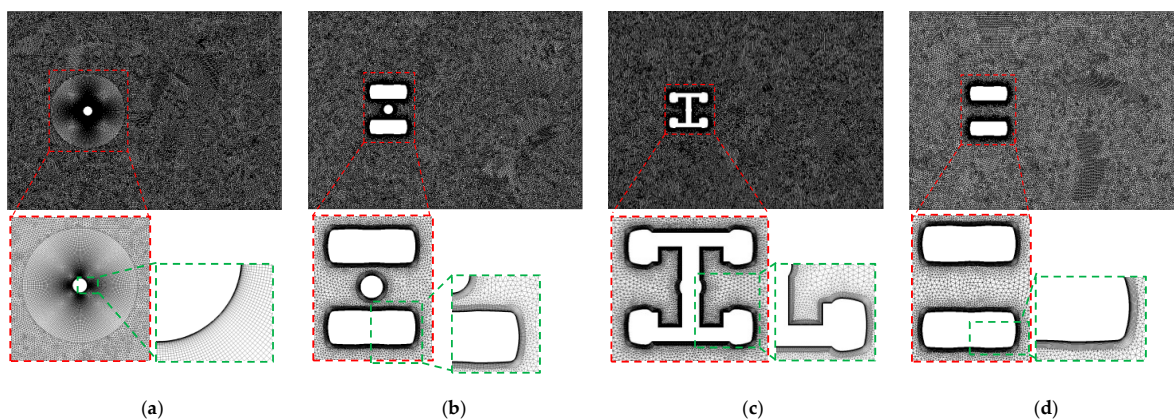


Figure 5. Mesh configurations of the LG C-Ss at: (a) Sec.1 or Sec.2; (b) Sec.3; (c) Sec.4; and (d) Sec.5.

The flow conditions used in all the simulations are based on the anechoic open wind tunnel [10]. The flow density,  $\rho_0 = 1.18 \text{ kg/m}^3$ , the static pressure,  $P_0 = 9.67723 \times 10^4 \text{ Pa}$ , and the inlet velocity,  $U_{in} = 78.99 \text{ m/s}$ , which corresponds to  $M = 0.23$ . The LES turbulence model is used for all the simulations. The solution is performed in the time domain by using an implicit second order scheme.

To enhance the solution accuracy and accelerate the simulations, the non-iterative time advancement scheme is used. The  $\Delta t$  is set to  $5.0 \times 10^{-6}$  s throughout the simulations to ensure numerical convergence and stability. In the case of the LES model,  $\Delta t$  size is governed by the time scale of the smallest resolved eddies. Thus, the Courant-Friedrichs-Lewy (CFL) number is maintained close to one. Based on this  $\Delta t$ , the highest frequency is 100 kHz. It is important to ensure that the flow exhibits a quasi-stationary behaviour before extracting the source data for the acoustic analysis.

Table 3 presents the summary of the location of each 2D C-S, all the calculated flow parameters, and their mesh properties. The  $Re^*$  for each C-S is determined based on the corresponding  $L_a$ . The LAGOON NLG has an inner cavity with side-to-side spacing,  $S = 198$  mm, and the wheel diameter,  $D_w = 300$  mm [10]. For the full 3D LG model, the  $Re = 1.56 \times 10^6$  is calculated based on the wheel diameter since it has the largest dimension in comparison to other components. Consequently, the flow behaves in the upper transition regime. In this study, the calculated  $Re^*$  has a wide range of flow regimes from critical lower transition to upper transition, including supercritical.

**Table 3.** Summary of flow parameters and mesh properties for the 2D C-Ss of the LAGOON NLG.

Case Name	Location along Z-axis, $L_z$ (m)	Characteristic Length, $L_a$ (m)	Aspect Ratio, $l/L_a$	$Re^*$	Compactness Condition Parameters			Source Correlation Length, SCL (m) ( $L_a \ll \lambda$ )	Mesh Size No. of Elements
					St	$f$ (Hz)	$\lambda$ (m)		
Sec.1	+0.335	$D_{c1} = 0.071$	6.366	$3.70 \times 10^5$	0.2 <sup>□</sup>	222.5	1.5	$5.0D_{c1} = 0.355$ $2.5D_{c1} = 0.178$ $0.8D_{c1} = 0.056^{\dagger}$	$8.11 \times 10^4$
Sec.2	+0.194	$D_{c2} = 0.055$	4.327	$2.86 \times 10^5$		287.2	1.2	$5.0D_{c2} = 0.275$ $2.5D_{c2} = 0.138$ $1.58D_{c2} = 0.087^{\dagger}$	$5.00 \times 10^4$
Sec.3	+0.104	$D_{w3} = 0.214$	—	$1.11 \times 10^6$		73.8	4.6	$2.5D_{w3} = 0.535$ $0.486D_{w3} = 0.104$ $0.107D_{w3} = 0.023$	$9.71 \times 10^4$
Sec.4	0	$D_{w4} = 0.300$	0.293	$1.56 \times 10^6$		52.7	6.5	$2.5D_{w4} = 0.751$ $0.347D_{w4} = 0.104$ $0.077D_{w4} = 0.023$	$1.35 \times 10^5$
Sec.5	-0.104	$D_{w5} = 0.214$	—	$1.11 \times 10^6$		73.8	4.6	$2.5D_{w5} = 0.535$ $0.486D_{w5} = 0.104$ $0.107D_{w5} = 0.023$	$7.29 \times 10^4$

<sup>†</sup> The value calculated based on the empirical formula (see Equation (2)).  $D_{c1}$  and  $D_{w3}$ —the subscripts “c” and “w” refer to the circular C-S and to non-circular C-S, respectively; whereas the number refers to the case number. <sup>□</sup> The St is assumed to equal to 0.2 based on the work of Roshko [30] for all C-Ss, in this study.

Note that the aspect ratio (AR),  $l_c/D_c$ , where,  $l_c$  and  $D_c$  are the cylinder length and diameter, respectively, is calculated only for Sec.1 and Sec.2. Both circular cylinders have larger aspect ratios than the wheel component. For the other C-Ss, each wheel also has a cylindrical geometry but with a shorter aspect ratio compared to the upper struts and with different orientation with respect to the incoming flow. In addition, these wheels are not smooth/continuous bluff bodies due to the inner and outer cavities. Thus, the aspect ratios of Sec.3 and Sec.4 are not computed, as illustrated in Table 3.

For each wheel body, the flow instabilities may occur in two different modes, lateral and longitudinal, as illustrated in Figure 6. The lateral perturbation could be generated due to the flow oscillation around the wheel along the Y-axis. The second longitudinal mode could be possibly generated due to the oscillatory motion of the flow around the Z-axis because of the wheel curvature. Since the wheel width is shorter than its length (i.e., diameter), the lateral instability may possibly occur first, and then may be coupled with the longitudinal mode. Similarly, the axle component has a cylindrical geometry, but the flow might only vibrate longitudinally. This is because it has different AR and orientation with respect to the cross-flow compared to the main and sub-set struts. Therefore, the proposed method only considers each component in an isolated manner, and no

interaction effect between the components of the LG is considered. Also, the 2D CFD simulations are limited to capture the lateral flow disturbance as a dominant source of noise.

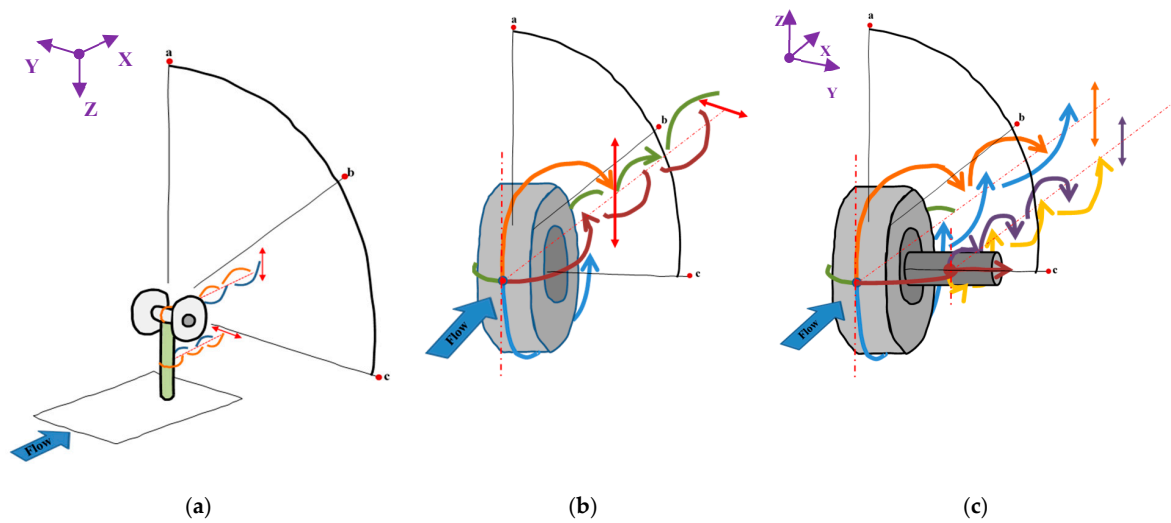


**Figure 6.** Schematic of possible flow instability modes occurring around: (a) the 3D LG model; (b) an isolated wheel; and (c) one wheel with axle component.

### 3.2. Acoustic Far-Field Computations for the LAGOON NLG

The far-field acoustic noise is computed using the built-in 3D FW-H solver in ANSYS FLUENT. For each C-S, the outer surface is assigned as an acoustic source. The source extracted from each 2D near-field flow domain is extended into the third dimension. This extension, along the spanwise direction, is elongated up to the assumed SCL to perform the FW-H surface integration. It implies that the data used in the third direction is identical to the source data collected from the 2D CFD simulation. Finally, the far-field acoustic pressure is collected at the receiver located right above each bluff body at 6 m distance. Since the source zone is specified at the solid surface of each body, only the surface integral of the FW-H equation is computed. Thus, only the dipole acoustic source due to the unsteady surface pressure fluctuations is included. Note that, the nonlinearity of the near-field is maintained; however, the effect of reducing the dimensionality of the flow domain on the prediction of the far-field noise is investigated.

The acoustic source of each resulting C-S is assumed to be acoustically compact. The compactness assumption is valid for  $L_a \ll \lambda$ , where  $\lambda$  is the acoustic wavelength. To get an initial estimate of  $St$ , there are empirical formulas presented by Norberg [21] for a wide range of  $Re$  (from 47 to  $3.0 \times 10^5$ ) of flow past a stationary circular cylinder. For example, Equation (1) is utilized in this study to estimate the  $St$  for Sec.1 and Sec.2.

$$St = 0.198 \left( 1 - \frac{19.7}{Re^*} \right) \tag{1}$$

The  $St$  magnitude is governed by Curle’s requirement [26] when  $St \ll 1/(2\pi M)$ . For Sec.1 and Sec.2 with  $M = 0.23$ ,  $St \ll 0.69$  to satisfy the compactness condition. It would be expected that the results captured at the main shedding tone ( $St \approx 0.2$ , from Equation (1)) and its harmonics would satisfy the Curle’s requirement. In addition, the empirical formula for estimating the SCL presented in [21] is also used. Based on the calculated  $Re^*$  for Sec.1 and Sec.2, as shown in Table 3, Equation (2) is used to calculate the SCL.

$$SCL = \left[ 1.4 \left( \frac{Re^*}{3.0 \times 10^5} \right)^{-2.7} \right] L_a \tag{2}$$

For Sec.3, Sec.4, and Sec.5, the SCL is assumed based on the geometric features of the two wheels and the corresponding  $Re^*$  of each C-S. The same number of acoustic pressure data is obtained for each C-S to calculate the total far-field noise. This corresponds to the unsteady pressure at the nodes of

the solid surface of each corresponding C-S. The total power spectral density (PSD) of all the noises propagated due to flow past those resulting C-S is calculated as:

$$PSD_{Total} = 10 \log_{10} \left( \sum_{i=1}^n 10^{PSD_i/10} \right) \tag{3}$$

where  $i$  is an index for the C-S number, and  $n$  indicates the total number of the C-Ss.

The total computation time for the near-field flow domain is  $t = 1.4010 \times 10^{-1}$  s. However, the FW-H solver is started after  $20 \times 10^3$  time steps, to ensure that the transient behaviour is settled, and run for further  $8.0 \times 10^3$  time steps to collect the acoustic data. The noise spectrum for each corresponding simulation is produced based on a total number of 3960 samples. The number of samples is kept the same to perform the summation and calculate the overall PSD noise level. It is worth highlighting that although the flow that generates the noise is usually nonlinear, unsteady, and turbulent, the radiated sound field is typically linear. In general, the far-field acoustic pressure is less than the atmospheric pressure. This implies that the superposition principle is valid [15]. Thus, the overall noise from the LAGOON NLG is obtained as the incoherent sum of the predicted noise from each C-S.

#### 4. The LAGOON NLG Results and Discussion

All the acoustic results presented are based on the multiple 2D C-Ss of the LAGOON NLG. First, the acoustic result of each 2D C-S is plotted considering three different values of the SCL to investigate its effect on the noise prediction. Then, the overall noise due to the contribution from each C-S is calculated and validated with the experimental and 3D numerical results.

##### 4.1. Multiple 2D Cross-Sections Acoustic Results

##### 4.1.1. The Upper Part of the LAGOON NLG

Figure 7 illustrates the effect of the SCL on the predicted far-field noise of Sec.1 and Sec.2. Three different values are assumed for SCL ( $SCL1 = 5.0D_{c1,2}$  and  $SCL2 = 2.5D_{c1,2}$ ) as suggested in previous studies of flow past a circular cylinder [21,22], whereas  $SCL3$  is estimated using Equation (2) for each C-S. Note that, the vortex shedding frequency,  $f$ , is calculated for all resulting C-Ss, as shown in Table 3. Roshko [30] demonstrated that for a wide spectrum of  $Re$  ( $2.0 \times 10^2 - 1.0 \times 10^5$ ), the vortex shedding frequency occurs at  $St \approx 0.2$ . Therefore, the  $St$  is assumed as 0.2 for all the 2D C-Ss.

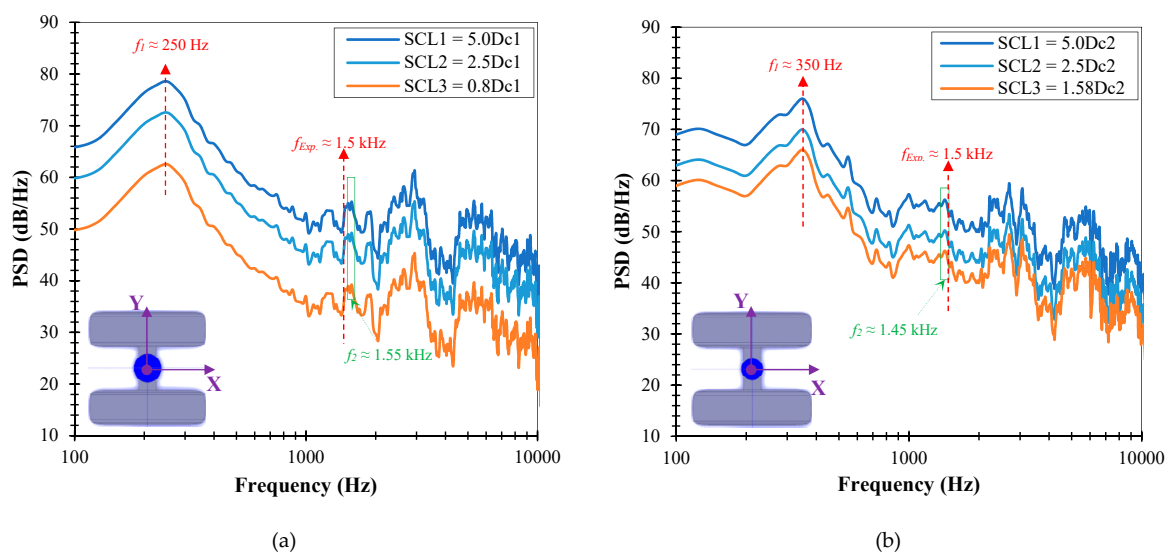


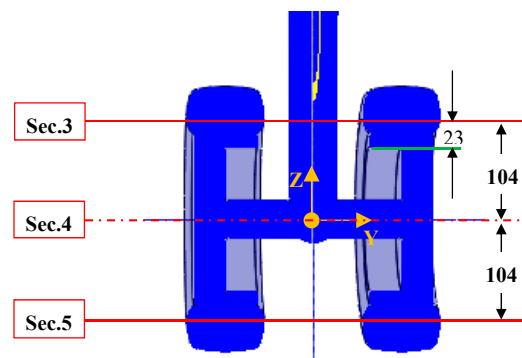
**Figure 7.** Effect of different SCL values on the acoustic prediction due to the upper part of the LAGOON NLG at: (a) Sec.1; and (b) Sec.2.

Overall, the results in Figure 7 show that the SCL affects the amplitude of the predicted noise spectrum. The PSD noise levels of different values of the SCL are within constant offset from each other. Figure 7a shows that the peak of the first harmonic of Sec.1 occurs at low frequency,  $f_1 \approx 250$  Hz, and exhibits a significant broadening. For Sec.2, the fundamental frequency is shifted to a higher frequency,  $f_1 = 350$  Hz (Figure 7b), because it has a smaller diameter than Sec.1. The first peak of the predicted noise is produced due to the fluctuating lift force around the resulting C-S.

It is interesting to note that some peaks are depicted around the tonal peak, as observed in the experiments at  $f_{Exp.} \approx 1.5$  kHz for the whole LG, as highlighted in Figure 7a,b. In Sec.1, the peak is slightly shifted to  $f_2 \approx 1.55$  kHz (Figure 7b), while for Sec.2, the peak is at  $f_2 \approx 1.45$  kHz (Figure 7b), and both are not sharp as seen during the experiments [12]. These peaks are not a tonal peak due to a cavity, but they could be produced due to a second harmonic frequency of the left force fluctuations.

#### 4.1.2. The Lower Part of the LAGOON NLG

The resulting C-Ss of the lower part of the current NLG have more complex configurations than the upper components. Therefore, the assumed values of the SCL avoid any abrupt changes in the geometry, such as cavities or curvatures. For example, in Sec.3, the value of  $SCL1 = 2.5D_{w3}$  is equivalent to the SCL2 of Sec.2. The second  $SCL2 = 0.486D_{w3}$  is defined based on the distance between Sec.3 and Sec.4 (i.e., equal to 0.104 m), as shown in Table 3. The SCL3 is chosen to be  $0.107D_{w3}$  to avoid exceeding the wheel inner cavities edges, which is located 0.023 m from Sec.3, as shown in Figure 8. The same strategy is applied for both Sec.4 and Sec.5 since they are also located in the axle-wheel region.



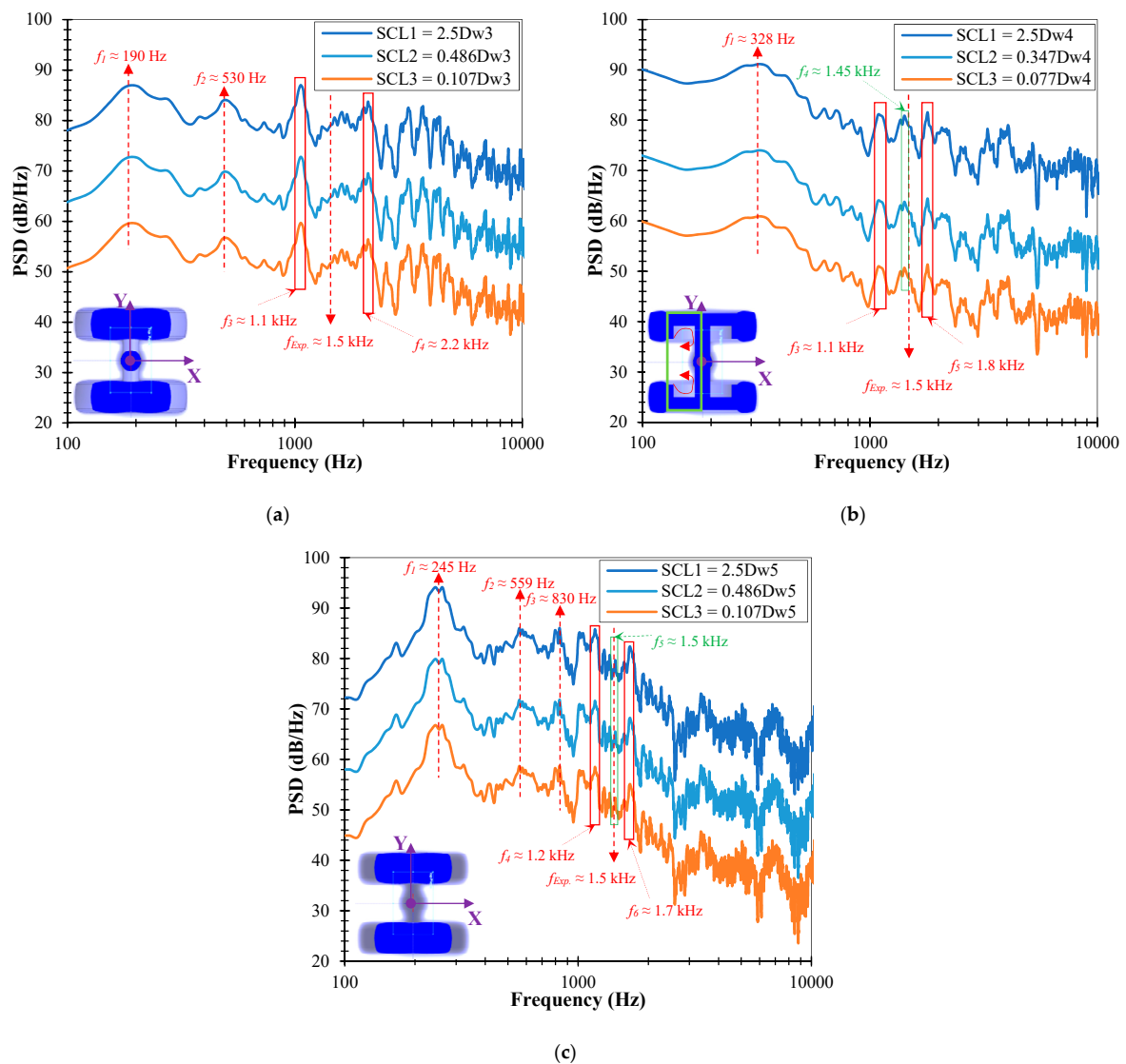
**Figure 8.** Locations and Z-level distances between Sec.3, Sec.4, and Sec.5 (all dimensions are in mm).

Table 3 presents three different SCL values for each C-S to investigate its effect on the predicted noise. Figure 9a–c illustrate the influence of assigning different SCL on the predicted noise obtained for Sec.3, Sec.4, and Sec.5, respectively. Similar to the results of Sec.1 and Sec.2, the PSD noise levels correspond to the SCL values considered are offset from each other, where the PSD curve due to SCL1 is the largest. It is worth noting that regardless of the shape of the resulting C-S, there is a proportional relationship between the assumed SCL and the predicted noise. Once the FW-H surface integration performed along a short length (i.e., assumed SCL), a noticeable reduction in the PSD noise spectrum was observed, as depicted in Figure 9a–c.

The acoustic result of Sec.3 reveals different tonal peaks, as shown in Figure 9a. This is because Sec.3 has two components. The first two peaks at  $f_1 \approx 190$  Hz and at  $f_2 \approx 530$  Hz may correspond to the vortex shedding generated by of the two-wheel upper C-S and the circular C-S of sub-set strut, respectively. The third and fourth tonal peaks at  $f_3 \approx 1.1$  kHz and  $f_4 \approx 2.2$  kHz may correspond to the flow interaction occurrence downstream after the flow past the entire C-S of Sec.3. It can be noted for Sec.3 that there is no peak at  $f_{Exp.} \approx 1.5$  kHz (Figure 9a). In contrast, for Sec.4, the tonal noise is visible at  $f_4 \approx 1.45$  kHz, as illustrated in Figure 9b. Moreover, two more peaks are evident, one before the experimental tonal noise at  $f_3 \approx 1.1$  kHz and the other at  $f_5 \approx 1.8$  kHz, as highlighted in Figure 9b.

These tones could be attributed to the flow impingement and circulation at the frontal portion of the inner cavities and the axle, as illustrated by the C-S of Sec.4 in Figure 9b.

Upon comparing Figures 9c and 9a, it can be noted that Sec.5 exhibits different peak frequencies compared to Sec.3 although they have similar C-Ss. For Sec.5, three peaks at  $f_1 \approx 245$ ,  $f_2 \approx 559$ , and  $f_3 \approx 830$  Hz are visible in the low frequency range. However, in the medium frequency and high frequency ranges, there is only one peak detected (at each range) at  $f_4 \approx 1.2$  kHz and  $f_6 \approx 1.7$  kHz, respectively, as shown in Figure 9c. Thus, this study highlights important insights about the noise contribution of each C-S to the overall noise of the LG. Based on these preliminary results, the SCL should be assumed as small as possible (i.e.,  $SCL \ll L_a$ ) to ensure that the flow coherence level is met. Therefore, the spectrum result of each C-S based on the SCL3 value is selected to obtain the overall noise of the LG.



**Figure 9.** Effect of different SCL values on the acoustic prediction due to the lower part of the LAGOON NLG at: (a) Sec.3; (b) Sec.4; and (c) Sec.5.

#### 4.2. The LAGOON NLG Overall Far-Field Acoustic Results

As mentioned above, the SCL3 is chosen to ensure that the FW-H integration is computed along where the flow is fully correlated. Figure 10a,b represent the PSD noise level of all the five C-S at different receiver locations (2D and 3D microphones), respectively, and compared with the experimental

data [12]. For the 2D microphone (2DMic), located at 6 m above the center of each C-S, some peaks are visible at the PSD results of Sec.1, Sec.2, and Sec.4 around  $f_{Exp.} \approx 1.5$  kHz, as illustrated in Figure 10a. However, for Sec.3 and Sec.5, no peaks are captured around  $f_{Exp.}$ . Figure 10b shows the PSD results of all the five C-Ss collected at 3D microphones (3DMic). The 3DMic is located in the sideline microphones arc (M6) at  $56^\circ$  from the flyover microphones arc as per the experimental measurements [12], as shown in Figure 10b. Based on these noise contributions from all the five C-Ss, the overall far-field noise is calculated using Equation (3).

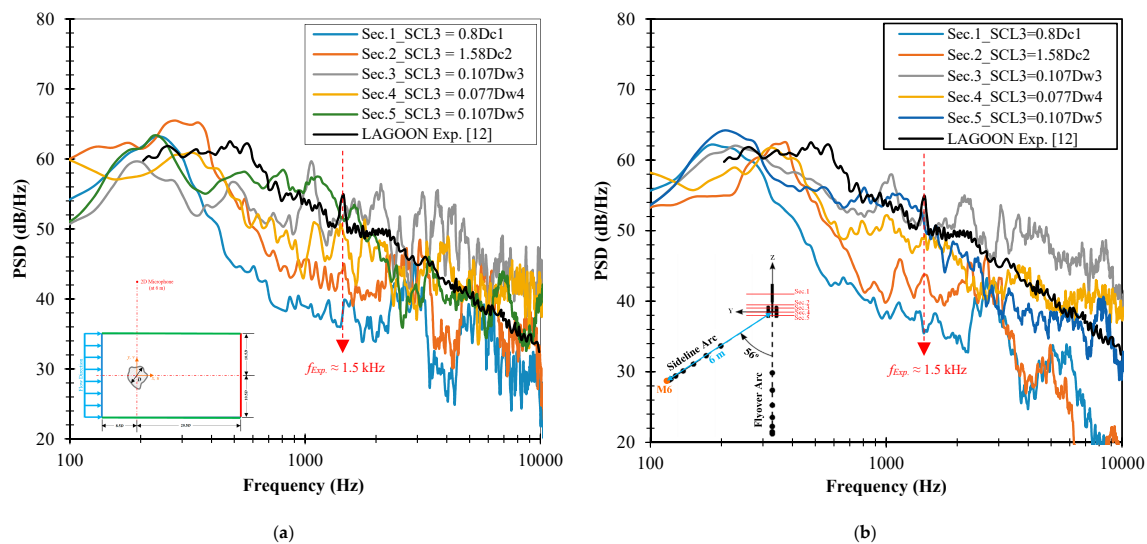


**Figure 10.** Comparisons of obtained PSD for all C-Ss of the LAGOON NLG with experimental results at: (a) 2D receiver locations relative to each domain; and (b) 3D microphone location at M6, as per the experiment.

Figure 11a presents the total PSD noise level of all the five C-Ss and compared them with the experimental [12] and 3D numerical results [44]. For the 2DMic, the result of the present approach has a good qualitative agreement with the experimental data at the medium-to-high frequency ranges (1.55–2.2 kHz), as illustrated in Figure 11a. It is important to note that, the tonal peak at  $f_{2D} \approx 1.02$  kHz captured by the 3D numerical results is successfully reproduced by the present study (for both 2DMic and 3DMic). However, this peak is not evident in the far-field noise experimental measurements. In fact, this tone was captured in the near-field unsteady surface pressure measurements conducted by Manoha et al. [12] using a Kulite<sup>®</sup> pressure transducer located at K15, as shown in the schematic diagram of Sec.4 in Figure 11a.

In contrast, Figure 11b shows the total PSD noise level obtained using the present approach at the 3DMic compared with experimental [12] and 3D numerical data [44]. The result of the 3DMic reveals a better qualitative matching with the experiment. It can be observed that a very tiny peak at  $f_{Exp.} \approx 1.5$  kHz is successfully captured, as shown in Figure 11b. This tonal peak would be more visible if the inner cavities are properly addressed, which can be tackled in the future. The effect of the microphone location on the noise prediction was also observed by Heller et al. [43]. Thus, the location of the receiver has a great influence on the amplitude and frequency of the far-field noise. Overall, the proposed approach can predict some of the peaks in reasonable agreement with the experimental data at a low computational cost. Each simulation takes about 10–16 h (i.e., 2–3 days for all the five 2D simulations) to obtain the acoustic data. The calculations were performed on a 64-bit, 3.60 GHz Intel<sup>®</sup> Core<sup>™</sup> i7-4790 with 32 GB of available memory.

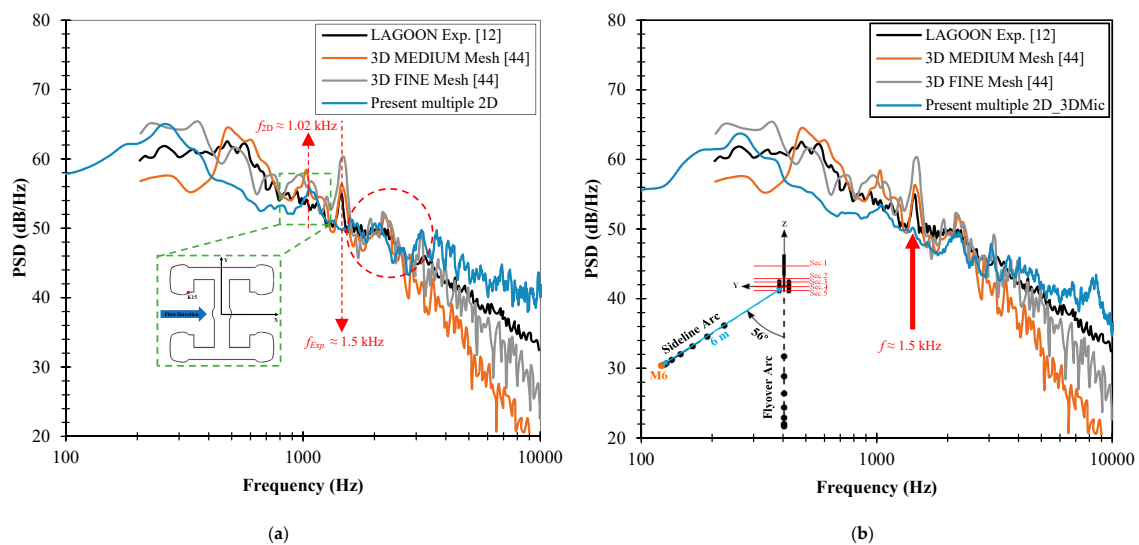


**Figure 11.** Comparison of the overall PSD based on the summation of all signals with experimental and 3D numerical data at: (a) 2D receiver locations relative to each domain; and (b) 3D microphone location at M6, as per the experiment.

## 5. Conclusions

This paper presented a new approach to predict the LG far-field noise based on near-field flow data obtained from multiple 2D simulations. The LG structure was divided into multiple 2D C-Ss to represent different configurations. The locations of these C-Ss are selected based on the number of components, sizes, and geometric complexities. The 3D FW-H acoustic analogy is used to calculate the far-field noise. The results of flow past a circular cylinder with  $Re = 9.0 \times 10^4$  using the 2D simulation showed that most of the flow quantities were reasonably reproduced while the  $St$  was over-predicted. For the LAGOON NLG, three different values for the SCL were investigated for each resulting C-S. For Sec.1 and Sec.2, the SCL3 was assumed in accordance with the utilization of the available empirical formula. However, for Sec.3, Sec.4, and Sec.5, the SCL3 was assumed to be smaller than the corresponding  $L_a$  to ensure that the FW-H integration is evaluated, assuming the flow is fully correlated. It was noted that different SCL resulted in a constant offset of the predicted noise level over the entire frequency spectrum. The predicted far-field noise based on the multiple 2D simulations was found to be in agreement with the experimental and 3D computational data. In addition, it was found that the location of the receiver influences both the amplitude and frequency of the predicted far-field noise. The results based on the 3DMic location showed a better agreement with the experimental data. This proves the ability of the proposed approach in capturing the aerodynamic noise relative to the far-field receiver location. The proposed approach provided a reasonable far-field noise prediction at a low computational cost. Thus, it could be utilized as a framework to assess the emitted noise of each LG components. In addition, this method has the potential to be used as a quick design tool to predict the noise impact of new LG designs. Also, one of the main advantages is that each individual acoustic result could be used to evaluate the contribution of each LG C-S to the overall noise level.

To further investigate the validity of the proposed approach, a more complex 3D LG model needs to be tested and validated with available experimental data. Overall, by approximating the fully 3D flow over the LG into multiple 2D models, the quasi-periodic vortex shedding generated due to each resulting C-S was visible. As a result, the unsteady loading on each C-S is considered as a primary source of noise generation for the LAGOON NLG. Note that, although the effect of the flow interaction between the C-Ss was not considered, some important peaks were successfully captured. Nevertheless, more investigations are needed to compensate for the 3D wake effect, which could be modified using the spanwise statistical modelling. In addition, when each LG component is assumed to have a compact C-S, the emitted noise could be predicted using the sectional lift and drag forces

directly. This will assess the contribution of each 2D C-S on the overall noise and which component of the LG is considered dominant.

**Author Contributions:** S.A. was responsible for developing the proposed method of dividing the LG into multiple 2D C-Ss. He was also involved in running all the simulations using ANSYS FLUENT, analyzing results, and the evaluation of each 2D C-S. He drafted the article, critically reviewed and implemented revisions. S.D. contributed to the presentation of results and critically reviewed this article. K.B. supervised all aspects of the research and critically reviewed this article.

**Funding:** This research was funded by the Natural Sciences and Engineering Research Council of Canada (NSERC under Discovery Grant No. RGPIN 217525).

**Acknowledgments:** The computations facility provided by the Advanced Research Laboratory for Multifunctional Lightweight Structures (ARL-MLS) at the University of Toronto is gratefully acknowledged. First author acknowledges Saudi Arabia government (Taibah University) for granting a scholarship to pursue the PhD degree.

**Conflicts of Interest:** The authors declare no conflict of interest.

## References

1. Busquin, P.; Argüelles, P.; Bischoff, M.; Droste BA, C.; Evans, R.H.; Kröll, W. European aeronautics: A vision for 2020—a synopsis. *Air Space Eur.* **2001**, *3*, 16–18. [[CrossRef](#)]
2. Dobrzynski, W. Almost 40 years of airframe noise research: What did we achieve? *J. Aircr.* **2010**, *47*, 353–367. [[CrossRef](#)]
3. Delfs, J.; Bertsch, L.; Zellmann, C.; Rossian, L.; Kian Far, E.; Ring, T.; Langer, S. Aircraft Noise Assessment—From Single Components to Large Scenarios. *Energies* **2018**, *11*, 429. [[CrossRef](#)]
4. Choudhari, M.M.; Yamamoto, K. Integrating Cfd, Caa, and experiments towards benchmark datasets for airframe noise problems. In Proceedings of the 5th Symposium on Integrating CFD and Experiments in Aerodynamics, Tokyo, Japan, 3–5 October 2012.
5. Lopes, L.V.; Redonnet, S.; Imamura, T.; Ikeda, T.; Zawodny, N.S.; Cunha, G. Variability in the Propagation Phase of CFD-Based Noise Prediction: Summary of Results from Category 8 of the BANC-III Workshop. In Proceedings of the 21st AIAA/CEAS Aeroacoustics Conference, Dallas, TX, USA, 22–26 June 2015; p. 2845.
6. Choudhari, M.; Lockard, D. Simulations measurements of airframe noise: A BANC workshops perspective. In Proceedings of the Specialists Meeting on “Progress and Challenges in Validation Testing for Computational Fluid Dynamics” (AVT-246), Zarazoga, Spain, 26–28 September 2016.
7. Singer, B.A.; Guo, Y. Development of computational aeroacoustics tools for airframe noise calculations. *Int. J. Comput. Fluid Dyn.* **2004**, *18*, 455–469. [[CrossRef](#)]
8. Farassat, F.; Casper, J. Towards an airframe noise prediction methodology: Survey of current approaches. In Proceedings of the 44th AIAA Aerospace Sciences Meeting and Exhibit, Reno, NV, USA, 9–12 January 2006; p. 210.
9. Schlottke-Lakemper, M.; Yu, H.; Berger, S.; Meinke, M.; Schröder, W. A fully coupled hybrid computational aeroacoustics method on hierarchical Cartesian meshes. *Comput. Fluids* **2017**, *144*, 137–153. [[CrossRef](#)]
10. Manoha, E.; Bulté, J.; Caruelle, B. LAGOON: An experimental database for the validation of CFD/CAA methods for landing gear noise prediction. In Proceedings of the 14th AIAA/CEAS Aeroacoustics Conference (29th AIAA Aeroacoustics Conference), Vancouver, BC, Canada, 5–7 May 2008; p. 2816.
11. Spalart, P.R.; Shur, M.L.; Strelets, M.K.; Travin, A.K. Initial noise predictions for rudimentary landing gear. *J. Sound Vib.* **2011**, *330*, 4180–4195. [[CrossRef](#)]
12. Manoha, E.; Bulté, J.; Ciobaca, V.; Caruelle, B. LAGOON: Further analysis of aerodynamic experiments and early aeroacoustics results. In Proceedings of the 15th AIAA/CEAS Aeroacoustics Conference (30th AIAA Aeroacoustics Conference), Miami, FL, USA, 11–13 May 2009; p. 3277.
13. Lockard, D. Summary of the tandem cylinder solutions from the benchmark problems for airframe noise computations-I workshop. In Proceedings of the 49th AIAA Aerospace Sciences Meeting including the New Horizons Forum and Aerospace Exposition, Orlando, FL, USA, 4–7 January 2011; p. 353.
14. Jenkins, L.; Khorrami, M.; Choudhari, M.; McGinley, C. Characterization of unsteady flow structures around tandem cylinders for component interaction studies in airframe noise. In Proceedings of the 11th AIAA/CEAS Aeroacoustics Conference, Monterey, CA, USA, 23–25 May 2005; p. 2812.

15. Lopes, L.V. A New Approach to Complete Aircraft Landing Gear Noise Prediction. Ph.D. Thesis, The Pennsylvania State University, State College, PA, USA, 2009.
16. Braza, M.; Chassaing, P.H.H.M.; Minh, H.H. Numerical study and physical analysis of the pressure and velocity fields in the near wake of a circular cylinder. *J. Fluid Mech.* **1986**, *165*, 79–130. [[CrossRef](#)]
17. Franke, R.; Rodi, W.; Schönung, B. Numerical calculation of laminar vortex-shedding flow past cylinders. *J. Wind Eng. Ind. Aerodyn.* **1990**, *35*, 237–257. [[CrossRef](#)]
18. Mittal, R.; Balachandar, S. Effect of three-dimensionality on the lift and drag of nominally two-dimensional cylinders. *Phys. Fluids* **1995**, *7*, 1841–1865. [[CrossRef](#)]
19. Belov, A.; Martinelli, L.; Jameson, A.; Belov, A.; Martinelli, L.; Jameson, A. Three-dimensional unsteady incompressible flow computations using multigrid. In Proceedings of the 35th Aerospace Sciences Meeting and Exhibit, Reno, NV, USA, 6–9 January 1997; p. 443.
20. Blackburn, H.M.; Melbourne, W.H. The effect of free-stream turbulence on sectional lift forces on a circular cylinder. *J. Fluid Mech.* **1996**, *306*, 267–292. [[CrossRef](#)]
21. Norberg, C. Fluctuating lift on a circular cylinder: Review and new measurements. *J. Fluids Struct.* **2003**, *17*, 57–96. [[CrossRef](#)]
22. Orselli, R.; Meneghini, J.; Saltara, F. Two and three-dimensional simulation of sound generated by flow around a circular cylinder. In Proceedings of the 15th AIAA/CEAS Aeroacoustics Conference (30th AIAA Aeroacoustics Conference), Miami, FL, USA, 11–13 May 2009; p. 3270.
23. Cox, J.S.; Brentner, K.S.; Rumsey, C.L. Computation of vortex shedding and radiated sound for a circular cylinder: Subcritical to transcritical Reynolds numbers. *Theor. Comput. Fluid Dyn.* **1998**, *12*, 233–253. [[CrossRef](#)]
24. Morkovin, M. Flow around circular cylinders—A kaleidoscope of challenging fluid phenomena. In Proceedings of the ASME Symposium on Fully Separated Flow, Philadelphia, PA, USA, 1964; pp. 102–118.
25. Kacker, S.C.; Pennington, B.; Hill, R.S. Fluctuating Lift Coefficient for a Circular Cylinder in Cross Flows. *J. Mech. Eng. Sci.* **1974**, *16*, 215–224. [[CrossRef](#)]
26. Doolan, C.J. Computational bluffbody aerodynamic noise prediction using a statistical approach. *Appl. Acoust.* **2010**, *71*, 1194–1203. [[CrossRef](#)]
27. Brentner, K.S.; Cox, J.S.; Rumsey, C.L.; Younis, B.A. Computation of sound generated by flow over a circular cylinder: An acoustic analogy approach. In *NASA Conference Publication*; NASA: Washington, DC, USA, 1997; pp. 289–296.
28. Casalino, D.; Jacob, M. Prediction of aerodynamic sound from circular rods via spanwise statistical modelling. *J. Sound Vib.* **2003**, *262*, 815–844. [[CrossRef](#)]
29. Revell, J.D.; Prydz, R.A.; Hays, A.P. *Experimental Study of Airframe Noise vs. Drag Relationship for Circular Cylinder*, Lockheed Report 28074; Final report for NASA Contract NAS1-14403. 1977.
30. Roshko, A. Experiments on the flow past a circular cylinder at very high Reynolds number. *J. Fluid Mech.* **1961**, *10*, 345–356. [[CrossRef](#)]
31. Cantwell, B.; Coles, D. An experimental study of entrainment and transport in the turbulent near wake of a circular cylinder. *J. Fluid Mech.* **1983**, *136*, 321–374. [[CrossRef](#)]
32. Vatsa, V.N.; Khorrami, M.R.; Park, M.A.; Lockard, D.P. Aeroacoustic simulation of nose landing gear on adaptive unstructured grids with FUN3D. In Proceedings of the 19th AIAA/CEAS Aeroacoustics Conference, Berlin, Germany, 27–29 May 2013; p. 2071.
33. Guo, Y.P. Application of the Ffowcs Williams/Hawkings equation to two-dimensional problems. *J. Fluid Mech.* **2000**, *403*, 201–221. [[CrossRef](#)]
34. Chekiri, R.; Lavoie, P.; Richarz, W.G. Experimental aeroacoustics of a two-strut, two-wheel landing gear in a propeller wake. In Proceedings of the 52nd Aerospace Sciences Meeting, National Harbor, MD, USA, 13–17 January 2014; p. 0020.
35. Curle, N. The influence of solid boundaries upon aerodynamic sound. *Proc. R. Soc. Lond. Ser. A Math. Phys. Sci.* **1955**, *231*, 505–514.
36. Manoha, E.; Caruelle, B. *LAGOON Simplified (2-Wheel) Nose Landing Gear Configuration #1 Experimental Database*, Technical Report R12; Funded by an aircraft supplier (Airbus-France), Version 1. 2011.
37. Liu, W.; Kim, J.W.; Zhang, X.; Angland, D.; Caruelle, B. Landing-gear noise prediction using high-order finite difference schemes. *J. Sound Vib.* **2013**, *332*, 3517–3534. [[CrossRef](#)]

38. Sanders, L.; Manoha, E.; Ben Khelil, S.; Francois, C. LAGOON: CFD/CAA coupling for landing gear noise and comparison with experimental database. In Proceedings of the 17th AIAA/CEAS Aeroacoustics Conference (32nd AIAA Aeroacoustics Conference), Portland, OR, USA, 5–8 June 2011; p. 2822.
39. Szepessy, S. On the spanwise correlation of vortex shedding from a circular cylinder at high subcritical Reynolds number. *Phys. Fluids* **1994**, *6*, 2406–2416. [[CrossRef](#)]
40. Evdokimov, I.; Kraposhin, M.; Strizhak, S. Implementation of acoustic analogy CAA in OpenFOAM. In Proceedings of the OpenFOAM 11th Workshop, Guimaraes, Portugal, 26–30 June 2016.
41. De la Puente, F.; Sanders, L.; Vuillot, F. On LAGOON nose landing gear CFD/CAA computation over unstructured mesh using a ZDES approach. In Proceedings of the 20th AIAA/CEAS Aeroacoustics Conference, Atlanta, GA, USA, 16–20 June 2014; p. 2763.
42. Rodarte Ricciardi, T.; Azevedo, P.; Wolf, W.; Speth, R. Noise Prediction of the LAGOON Landing Gear Using Detached Eddy Simulation and Acoustic Analogy. In Proceedings of the 23rd AIAA/CEAS Aeroacoustics Conference, Denver, CO, USA, 5–9 June 2017; p. 3010.
43. Heller, H.H.; Dobrzynski, W.M. Sound radiation from aircraft Wheel-WelV Landing-Gear configurations. *J. Aircr.* **1977**, *14*, 768–774. [[CrossRef](#)]
44. Giret, J.C.; Sengissen, A.; Moreau, S.; Jouhaud, J.C. Prediction of LAGOON landing-gear noise using an unstructured LES Solver. In Proceedings of the 19th AIAA/CEAS Aeroacoustics Conference, Berlin, Germany, 27–29 May 2013; p. 2113.
45. Demartino, C.; Ricciardelli, F. Aerodynamics of nominally circular cylinders: A review of experimental results for Civil Engineering applications. *Eng. Struct.* **2017**, *137*, 76–114. [[CrossRef](#)]



© 2019 by the authors. Licensee MDPI, Basel, Switzerland. This article is an open access article distributed under the terms and conditions of the Creative Commons Attribution (CC BY) license (<http://creativecommons.org/licenses/by/4.0/>).